This is the Pre-Published Version.

This is the peer reviewed version of the following article: Yang, C., Huang, B., Bai, S., Feng, Y., Shao, Q., Huang, X., A Generalized Surface Chalcogenation Strategy for Boosting the Electrochemical N2 Fixation of Metal Nanocrystals. Adv. Mater. 2020, 32, 2001267, which has been published in final form at https://doi.org/10.1002/adma.202001267. This article may be used for non-commercial purposes in accordance with Wiley Terms and Conditions for Use of Self-Archived Versions. This article may not be enhanced, enriched or otherwise transformed into a derivative work, without express permission from Wiley or by statutory rights under applicable legislation. Copyright notices must not be removed, obscured or modified.

A General Strategy to Boost the Electroreduction of N_2 via Surface Chalcogenation of Metal Nanocrystals

Chengyong Yang,[1,+] Shuxing Bai,[1,+] Yonggang Feng,[1] Bolong Huang,[2,*] Ting Zhu,[1] Qi Shao,[1] and Xiaoqing Huang[1,*]

[1]College of Chemistry, Chemical Engineering and Materials Science, Soochow University, Jiangsu 215123, China.

[2]Department of Applied Biology and Chemical Technology, The Hong Kong Polytechnic University, Hung Hom, Kowloon, Hong Kong SAR.

[+]Chengyong Yang and Shuxing Bai contributed equally to this work.

*To whom correspondence should be addressed.

E-mail: bhuang@polyu.edu.hk, hxq006@suda.edu.cn

Abstract: The elusive goal has been long for efficient nitrogen-reduction towards high yield ammonia, where there is a greatly challenge, how do we activate inert nitrogen conversion under ambient environments? This sluggish path leads us towards finding out or accomplishing near-barrier-free initiation of self-sensitization of that chosen electrocatalyst. It has to be admitted that the traditional electrocatalysts have uncertain structure and valence state, which in fact bring the key challenge in the nitrogen reduction reaction. Herein, for the first time, we have presented a robust surface chalcogenation strategy to prominently boost the NRR performance of normal transition metal nanocrystals. Surprisingly, the NH_3 yield and FE (175.6 mg h^{-1} g^{-1}_{Rh} and 13.3%)

The article must be linked to Wiley's version of record on Wiley Online Library and any embedding, framing or otherwise making available the article or pages thereof by third parties from platforms, services and websites other than Wiley Online Library must be prohibited.

of the surface selenated Rh NCs (Rh-Se NCs) has been significantly enhanced by 16 and 19 times fold, respectively, indicating an efficient electroactivity optimization. Moreover, the durability of such surface modulation has been verified by the long-term electrolysis and consecutive reactions. Theoretical calculations reveal the intrinsic mechanism of this efficient strategy, in which the interfacial strain effect from surface chalcogenation activates the critical redox inversion of Rh. This results in relatively low valence states of Rh and Se surface sites with *p-d* band-merged, which actualize an efficient electron-transfer with minimized NRR barriers. Thus, the volcano-like correlation between the surface chalcogenation shell strain and electronic activities intrinsically guarantees the high NRR catalytic activities. Most importantly, this work has presented an efficient surface chalcogenation strategy with universality to enhance the electroactivity towards NRR for broad transition metal nanocrystal electrocatalysts. This rational design and tailoring strategy open an exciting new avenue for future production of ammonia for a breakthrough in the conversion bottleneck of NRR under ambient conditions.

Ammonia (NH_3) is a vital building block to the global economy to synthesize a wide range of crucial chemicals including fertilizer, clean energy carrier, and hydrogen storage molecule, etc.[1–5] However, due to the extremely stable N≡N bond, the present industrial production of NH_3 still relies on the "high-temperature, high pressure" Haber-Bosch process (HBP) from highly pure N_2 and H_2, which requires intensive energy and capital cost. [6–7] More importantly, the preparation of highly pure H_2 largely depends on the steam reforming of natural gas from fossil fuels, which result in intenseemission of greenhouse gases and continuous consumption of non-renewable resources, etc.[8–10] Thus, the replacement of traditional HBP through the robust and heterogeneous carbon-free catalyst is highly

demanded for the increasingly serious environmental problems and growing depletion of fossil fuels. Beyond the synthesis of a single novel electrocatalyst with remarkable performance, the development of the highly efficient NRR electrocatalyst strategy is critical to accelerate the transition of HBP to more environmental-friendly N_2 fixation process.

The ever-increasing demands for facile synthetic NH_3 have stimulated numerous efforts to develop alternative routes for artificially fixing N_2 by using biological nitrogenase, photocatalysis, and electrocatalysis.[11–13] Among these options, electrochemical reduction of N_2 towards NH_3 has gained paramount importance, since it not only can be powered by the renewable energy but also operate under atmospheric pressure by utilizing earth abundant resources water (H_2O) as the hydrogen source.[14–16] However, electroreduction of N_2 is still severely challenged by weak bonding of initial N_2 adsorption and arduous N≡N activation.[17] To breakthrough the low efficiency of NRR, a variety of nanomaterials have been explored as NRR electrocatalysts including metal-based catalysts (Au,[18] Ru,[19–20] Pd,[21] Rh,[22] etc.), metal compounds (Fe_2O_3,[23] $W_{18}O_{49}$,[24] MnO,[25] etc.) or even metal-free catalysts (B_4C, [26] N-doped porous carbon,[27] black phosphorus nanosheets,[28] etc.). To date, after careful electrocatalysts experimental and theoretical screening with different compositions and structures, a series of metal-based electrocatalysts have been designed and fabricatedbecause of their unique electronic structure, excellent catalytic activity, and low overpotential.[29] Though impressive progress has been achieved in the past few years, the NRR electrocatalyst still lacks systematic developments to boost efficiency in a general approach. Moreover, the competitive hydrogen evolution reaction (HER) process is also well-known that further leads to the comprising NRR yields and faradic efficiency. Thus, developing a facile and reliable strategy to enhance the activity and FE for NRR of metal-based catalysts indeed matters for the green and sustainable NH_3 production.

As the core of electrocatalyst, the surface morphology determines their essential electronic properties for achieving optimal adsorption energies, reduced activation barriers and sufficient active sites for intermediates.[30] Thus, the appropriate surface modification of the metal-based catalyst is of pivotal significance to activate a boosting effect to improve NRR performance. Herein, we report a universal and efficient surface chalcogenation strategy on metal nanocrystals (NCs) to fabricate the highly robust NRR electrocatalysts with substantially improved activity, FE and durability at ambient conditions. Far beyond the pure metal NCs, the surface chalcogenated metal NCs exhibit a pronounced increase in NH_3 production rate and FE towards NRR owe to the enhanced adsorption of N_2 and evident suppression of HER process. Most significantly, the optimized surface selenated Rh NCs (Rh-Se NCs) exhibit excellent NRR performance in 0.10 M HCl, in which high NH_3 yield with 175.6 mg h^{-1} g^{-1}_{Rh} and a high FE with 13.3% is actualized.This remarkable performance outperforming the original Rh NCs by 16 and 19 times in NH_3 yield and FE, respectivley. The developed nanocatalysis system also shows excellent stability, where both the NH_3 yields and FE displays negligible changes of the catalysts after five reaction rounds and 18 h electroreduction at -0.10 V vs. RHE. DFT calculations indicate a positive correlation between the catalytic and electronic activities in amorphous RhSe capped Rh-Se NCs system, regarding the interfacial strain effect incorporation. Within shell strain modulating trend, the anomalous redox inversion plays a critical role for merging Rh-4d and Se-4p bands on the surface. On the Rh-Se NCs surface, the Se-sites promote the electron-transfer rate between N-species and nearby Rh-sites. Meanwhile, the Se-sites with redox inversed are assisting to stabilize the lower valence of Rh-site for preserving such high electronic activities. This is the essential key promotion accomplishing a high electronic activity and NRR performance simultaneously.This work represents a new direction of enhancing the general NRR electoacitivty .

Results and discussion

Synthesis and structural characterization of Rh-Se NCs. The Rh-Se NCs were prepared through a two-step post-modification approach (**Figure 1a**). In the first step, we synthesized the uniform Rh NCs by reducing rhodium chloride ($RhCl_3$) with phenol in ethylene glycol (EG) solution. **Supplementary Figure 1a** shows representative transmission electron microscopy (TEM) of the prepared Rh NCs that confirms the monodispersion of synthesized NCs. The crystalline nature of the Rh NCs was further characterized by high-resolution TEM (HRTEM, **Supplementary Figure 1b**), where the interplanar spacing is measured to be 0.19 nm, assigned to the (200) plane of face-centered cubic (*fcc*) Rh (JCPDS number 05-0685). These as-prepared Rh NCs were utilized as the growing seeds for the Rh-Se NCs with surface selenation (**Figure 1a**). Typical high-angle annular dark-field scanning TEM (HAADF-STEM) image (**Figure 1b**) and TEM image (**Figure 1c**) verify the preservation of original morphology of Rh inthe Rh-Se NCs after surface selenation. The Rh/Se composition in Rh-Se NCs is 67.7/32.3, as confirmed by scanning electron microscope-energy spectrum analysis (SEM-EDS, **Supplementary Figure 2a**). The X-ray photoelectron spectroscopy (XPS) pattern was further carried out to examine the surface electronic properties of Rh-Se NCs. Apparently, two peaks located at 54.6 and 55.7 eVare assigned to Se_2^{2-} $3d_{5/2}$ and Se_2^{2-} $3d_{3/2}$ peaks,[31] supporting the existence of surface Se on the synthesized Rh-Se NCs (**Figure 1d**). The increase of Se composition on the Rh-Se NCs surface of produced NCs demonstrates an enrichment of Se in the surface, which has increased from 32.3 % to 49.2%, as confirmed by XPS. Interestingly, the powder X-ray diffraction (PXRD) pattern of Rh-Se NCs (**Figure 1e**) further illustrated the well-preserved *fcc* Rh based on the index of representative diffraction peaks at 41.1, 47.8, 69.8, 84.4 and 89.1º to (111), (200), (220), (311) and (222)surfaces. To further figure out the detailed structure of the Rh-Se NCs, HRTEM images for Rh-Se NCs were collected (**Figure 1f–h**). It is obvious that there is an amorphous shell surrounding the crystalline core (**Figure 1f**). The lattice spacing of the crystalline core shown in the HRTEM image (**Figure 1h**) is 0.19 nm, closing to that of the (200)

plane of Rh. Moreover, the HRTEM (**Figure 1g**) identified the sourrounding amorphous shell with a thickness of approximately 1.3 nm.. Through the peak widths using the Scherrer formula (**Supplementary Figure 3**), we discover a the average crystalline sizes of Rh NCs decreases in the Rh-Se NCs from ~ 10.7 to ~ 8.6 nm, respectively, due to the presence of amorphous RhSe shell. The Rh-Se NCs were also investigated by the HAADF-STEM elemental mapping (**Figure 1i**) and HAADF-STEM line scan (**Supplementary Figure 2b**), where the overlapped Rh and Se elemental image shows that Rh mainly locates in the core NCs while Se is enriched in the outer amorphous shell. Based on the above results, we systematically identified the components of core-shell structure of slenated Rh-Se NCs.

Electrochemical performance of Rh-Se NCs/C. The electrochemical measurements were performed in a two-compartment electrochemical cell in 0.10 M HCl under ambient conditions. N_2 gas is supplied in a feed gas stream to the cathode, where N_2 and H^+ combine with electrons to form N_2 reduction product (**Figure 2a**). To confirm the successful N_2 electroreduction in 0.10 M HCl, the produced NH_3 was spectrophotometrically determined by the indophenol blue method, and the possible by-product N_2H_4 was detected using the method of Watt and Chrisp[ref?]. To highlight the advantages of surface selenization strategy (Rh-Se NCs/C, **Supplementary Figure 4a–b**), the Rh NCs/C (**Supplementary Figure 4c–d**), Se NCs/C (Inset is PXRD pattern, **Supplementary Figure 4e–f**) and commercial Rh/C (**Supplementary Figure 4g–h**) were used as references to compare their NRR performances in N_2-saturated 0.10 M HCl electrolyte. **Supplementary Figure 5–8** presents the UV-vis absorption spectra of the various electrolytes after electrocatalytic reaction for 2 h at different potentials ranging from -0.05 V to -0.25 V vs. RHE under N_2 bubbling. Based on the calibration curves (**Supplementary Figure 9a–b**), the relationship between NH_3 production rate, FE and applied potential are plotted in **Figure 2b–c & Supplementary Figure 5**, respectively. Obviously, Rh NCs/C, Rh/C and Se NCs/C exhibit relatively poor activities for NRR (**Figure 2b–c & Figure S5b**), where Rh NCs/C (-0.10 V vs. RHE), Rh/C (-0.10

V vs. RHE) and Se NCs/C (-0.7 V vs. RHE) exhibit the overall ultra-low FE (< 1%) with NH_3 yields of only 11.0 mg^{-1} h^{-1} g^{-1}_{Rh}, 23.6 mg^{-1} h^{-1} g^{-1}_{Rh} and 2.2 mg h^{-1} g^{-1}_{cat}, respectively. In contrast to the reference catalysts, the NH_3 production rate of Rh-Se NCs/C significantly increases between -0.05 V and -0.25 V vs. RHE and reaches a maximum at -0.10 V vs. RHE of impressive 175.6 mg^{-1} h^{-1} g^{-1}_{Rh} (**Figure 2b & Supplementary Figure 6**). This yield has outdistanced those reference catalysts as large as nearly 80 times. More surprisingly, the high FE of 13.3% is achieved for Rh-Se NCs/C, at leasr one order higher than those references (< 1%, **Figure 2c**). Strikingly, at various applied potentials, Rh-Se NCs/C exhibit higher partial current densities of NH_3 production than that of other three catalysts, further confirming that the surface selenation of Rh NCs greatly enhance the catalytic properties of NRR (**Figure 2d & Supplementary Figure 5d**). No hydrazine has been detected (**Supplementary Figure 9c–d & Supplementary Figure 10**), indicating excellent selectivity for NRR toward NH_3. Below -0.10 V vs. RHE, the production rate, and FE decrease significantly, which is attributed to the domination of the competing HER process in this catalytic system. In addition, to guarantee the N sources of the product in NRR of Rh-Se NCs/C, several control experiments are performed (**Figure 2e & Supplementary Figure 11a**), including carbon support in N_2-saturated solution at -0.10 V vs. RHE, the Rh-Se NCs electrode in Ar-saturated solution at -0.10 V vs. RHE and at an open circuit. The corresponding UV-vis spectra and NMR for all control samples show weak signals comparable to that of the fresh electrolyte. Moreover, XPS excludes the existence of N source in Rh-Se NCs/C (**Supplementary Figure 11b**). In addition, the ^{15}N isotopic labeling experiment could be further proof that the N of produced NH_3 originated from the feed gas. Obviously, only $^{14}NH_4^+$ and $^{15}NH_4^+$ can be detected by NMR when $^{14}N_2$ and $^{15}N_2$ were used as the N source, respectively (**Supplementary Figure 12**). Those control experiments strongly support that the Rh-Se NCs/C are playing the critical role as the active species for catalyzing the electroreduction of N_2.

Electrochemical durability of Rh-Se NCs/C for NH_3 synthesis. The excellent durability of Rh-Se NCs/C during the electrochemical NRR process has been proved. As shown in **Figure 2f**, NH_3 production rate and FE of the Rh-Se NCs/C show slight changes during 5 times consecutive recycling tests at -0.10 V vs. RHE. Furthermore, under sustained N_2 gas flow, 18 h electrolysis at a potential of -0.10 V vs. RHE only leads to subtle decrease in current with nearly unchanged NH_3 production rate of about 179.2 $mg^{-1}\ h^{-1}\ g^{-1}_{Rh}$ (**Supplementary Figure 13**), which demonstrates the well-maintenance of that high electrocatalytic activity for NRR. The catalysts after recycling experiments (**Supplementary Figure 14**) were also characterized by means of tools, where the morphology, composition and surface properties of Rh-Se NCs/C have no obvious changes, further revealing that the reliable and stable electroreduction of N_2 by Rh-Se NCs/C.

Surface selenation effect. The surface characterization reflects crucial information about the surface properties of the electrocatalyst. To evaluate of the influence induced by the surface selenation, we compared the NH_3 production rate at different reaction temperatures to estimate the apparent activation energy (E_a). As shown in **Figure 3a**, the NH_3 production rate exhibits an increasing trend with the reaction temperature. Specifically, at -0.10 V vs. RHE, the NH_3 yields of Rh-Se NCs/C and Rh NCs/C gradually increase from 166.3 and 13.1 $mg^{-1}\ h^{-1}\ g^{-1}_{Rh}$ at 20 °C to 274.5 and 41.0 $mg^{-1}\ h^{-1}\ g^{-1}_{Rh}$ at 60 °C, respectively. The estimationof E_a of Rh-Se NCs/C and Rh NCs/C for the NRR are 11.5 and 23.2 kJ mol^{-1}, respectively (**Figure 3b**), which demonstrates the obviously reduced barrier of NRR by the facilitation of surface selenation in Rh-Se NCs .

Since the HER process is the main competing side reaction for the NRR in aqueous solutions, the HER properties and H_2 FE of Rh NCs/C and Rh-Se NCs/C were systematically explored. As shown in **Figure 3c & Supplementary Figure 15,** the Rh NCs/C exhibit substantially higher activity than Rh-Se NCs/C for HER, where the overpotentials of the Rh NCs/C and Rh-Se NCs/C reach 42 and 126 mV at a

current density of 10 mA cm^{-2}, respectively. Moreover, the Tafel slope of Rh-Se NCs/C (77.3 mV dec^{-1}) is higher than that of Rh NCs/C (49.2 mV dec^{-1}), revealing a kinetically suppressed HER. Similarly, in NRR, the H_2 FEs of Rh NCs/C and Rh-Se NCs/C at potentials between -0.05 V and -0.25 V vs. RHE are plotted in **Figure 3d**. Notably, Rh NCs/C exhibit ultrahigh H_2 FE ~ 100 % while the selenated Rh-Se NCs/C remarkably decreases the H_2 FE at all applied potentials. These results evidencedthe efficient inhabitation of the HER process by our proposed surface selenation strategy.

Surface characterization of Rh-Se NCs/C. To understand their enhanced NRR activity, the electronic structure of Rh NCs/C and Rh-Se NCs/C are also critical to investigate (**Figure 4a–b**). As shown in Rh 3d XPS (**Figure 4a**), it can be seen that two strong peaks of Rh NCs/C are located at 307.3 eV and 312.1 eV, corresponding to Rh^0 $3d_{5/2}$ and Rh^0 $3d_{3/2}$. Meanwhile, the two weak shoulder peaks at 308.3 and 313.1 eV belong to Rh^{3+} $3d_{5/2}$ and Rh^{3+} $3d_{3/2}$, respectively.[32] However, a slight shift of the Rh^0 $3d_{5/2}$ peak toward higher value (307.6 eV and 312.4 eV) is observed for the Rh-Se NCs/C compared with Rh NCs/C, indicating the electron transfer from Rh to Se. The asymmetry and tailing of Rh 3d XPS on Rh-Se NCs/C become more apparent than on that on Rh NCs/C, suggesting additional Rh^{3+} species formed after surface selenation of Rh NCs/C. The surface valance band spectra of Rh NCs/C and Rh-Se NCs/C were also collected by XPS. The modulated electronic effect (described by the *d*-band center with regard to Fermi level) further tunes the binding strength of NRR intermediates, which eventually modulates the catalytic activity.[33] As shown in **Figure 4b**, the upshift of the *d*-band center of gravity after introducing Se (Rh-Se NCs/C) was observed, compared with Rh NCs/C, thereby likely strengthening the adsorption of N_2 intermediate.[34] As shown in **Figure 4c**, the desorption peak is located at 421 °C, which is assigned to the chemical adsorption of N_2 on Rh-Se NCs/C. In contrast, the peak of Rh NCs/C for N_2 chemical adsorption is located at 370 °C. Therefore, the binding strength of N_2 on Rh-Se NCs/C has been largely reinforced than that on Rh NCs/C, supporting optimized N_2 adsorption by the surface

selenation of Rh NCs , thus resulting in the high activity of Rh-Se NCs/C. With the detailed experimental proofs and analysis, we conclude that the superior NRR performance of Rh-Se NCs/C is derived from the synergistic effect of enhancement of N_2 adsorption and inhibition of HER (**Figure 4d**).

Theoretical investigation. We further carried out DFT calculations to interpret the mechanism of high NRR performance given by the core@shell system. The shell layer consists of amorphous RhSe (a-RhSe) where the interface has been highly selenated based on the Rh (100) surface (**Figure 5a**). The bonding and anti-bonding orbitals near the Fermi level (E_F) have been demonstrated. It is clearly shown that the a-RhSe shell layer plays an electron-rich character from in-depth region towards top surface areas (**Figure 5a**). The Rh-4d band variation behavior has been studied. From the top surface Rh-site towards to the in-depth region, the dominant peak position of Rh-4d band has downshifted from E_V-0.9 eV to E_V-3.1 eV. The Rh-4d band center has also denoted a downshifting with 1.2 eV below the E_F to avoid possible (Rh-H)-over-binding effects (**Figure 5b**). For the Se-4p band variation trend, the 4p-band center has notably upshifted from E_V-7.0 eV to E_V-2.0 eV, from in-depth interfacial selenation sites towards top surface area, respectively. Within this trend, the role of Se-4p band in spatial view has turned from electron-capturing towards electron-depletion centers from deep selenation sites near Rh-core region towards shell surface. This variation trend evidently shows an inversion of redox states of Se-sites from oxidative to reducing characters changing within such core@shell system (**Figure 5c**). We further analyze the significance of such packing strategy in terms of core@shell particles. Due to the shell layer strain effect, the Se-4p and Rh-4d bands from Rh-Se NCs are nearly merged within same region indicating an efficient *p-d* coupled electron-transfer behavior, which robustly maintains the lower valence states of top surface Rh-sites for active catalysis (**Figure 5d**). To understand the shell strain effect, the elastic strain moduli of the core@shell system are described in terms of Lamé parameters within the realm of simplified continuum mechanics. The Rh-4d band center and strain modulus is

correlated in a volcano plot. From small to medium-scale modulus, the positive correlation shows the Rh-4d electronic activities increase. Towards ultra-large strain effect, the over-strong amorphization downgrades the Rh-4d electronic activities and suppresses the Rh-4d band center (**Figure 5e**). PDOSs analysis on the adsorbing N-species has been denoted on the Rh-Se NCs surface. With forwarding the N-hydrogenation, the s-orbital electronegativity presents a linear downward trend, indicating a substantial efficiency of electron-transfer and highly selectivity controlling space for N-reduction catalysis on the Rh-Se NCs surface (**Figure 5f**). Charge density slices also demonstrate the surface electronic states of Rh-Se NCs are long-range sensitive, which sensitizes the long-pair s-electronic orbitals of itinerant N_2 molecule. This guarantees a high rate of N_2-fixation (**Figure 5g**). Surface electronic work function has also been tested, which represents the electron-transfer capabilities from surface towards to adsorbing species. From our calculation, such capabilities are described in the order of Rh-Se NCs strain surface > Rh-Se NCs interface > plain RhSe surface > Rh (100) surface (**Figure 5h**).

Further viewing on energetic trend of NRR pathway, we find the overall energetic gain is -0.41 eV and energetic favorable with most steps in downhill trend. The overall energetic gain has been further transformed into the electrode potential between -0.048 V and -0.067 V, which show a good agreement with experimental measurement. The dominant barrier at U = -0.048 V is denoted at the step of forming $*NH_2 + NH_3 + (H^+ + e^-)$ from $*NH + NH_3 + 2(H^+ + e^-)$, which is 0.11 eV at the U = 0 V (**Figure 6a**). From local structural configurations (**Figure 6b**), we find all N-species are energetically favorable adsorbing on the lower coordinated Rh-site surrounding by both Rh and Se sites, while the nearby Se-sites without Se-Se bond play an enhanced electron-proton exchange center for re-distributing the H-species representing a rather high selectivity.

Generality of NRR enhancement on metals NCs by surface chalcogenation. To explore the versatility of the surface chalcogenation strategy of metal NCs for NRR, we extended the examination of other chalcogenated Rh NCs under the same catalytic conditions. As shown in **Figure 7a**, Rh-S NCs/C (**Supplementary Figure 16 & Supplementary Figure 19**) and Rh-Te NCs/C (**Supplementary Figure 17 & Supplementary Figure 19**) can readily achieve higher NRR performance than Rh NCs/C. At -0.10 V vs. RHE in 0.10 M HCl, the NH_3 production rate and FE of Rh-S NCs/C and Rh-Te NCs/C (**Figure 5a & Supplementary Figure 18**) reach peak value as high as 99.5 $mg^{-1}\ h^{-1}\ g^{-1}_{Rh}$ (FE: 6.1%) and 127.1 $mg^{-1}\ h^{-1}\ g^{-1}_{Rh}$ (FE: 9.2%), which is about 9.0 (8.7) folds and 11.6 (13.2) folds higher than that of Rh NCs/C, respectively. Importantly, the strategy of surface selenation in Rh NCs for improved catalytic properties is general and can be readily extended to other metals (Pt, Pd and Ru, **Supplementary Figure 19**) and even commercial Rh/C. We summarized the NH_3 yields and FE for these catalysts at -0.10 V vs. RHE in 0.10 M HCl (**Figure 7b–d**). Notably, it shows that M-Se NCs/C (M = Pt, Pd, Ru) efficiently suppress the HER process (**Figure 7b**). As shown in **Figure 7c–d**, compared with Rh/C and pure metal NCs/C, the NH_3 yield and FE of Rh/C-Se and M-Se NCs/C achieve the pronounced increase. At -0.10 V vs. RHE, the NH_3 yield and FE of Rh/C-Se, Pt-Se NCs/C, Pd-Se NCs/C and Ru-Se NCs/C reach as high as 109.3 (FE: 4.9%), 130.7 (FE: 3.7%), 84.3 (FE: 6.4%) and 80.7 (FE: 3.2%) mg $h^{-1}\ g^{-1}$, which is about 4.6 (10.2), 3.5 (52.9), 4.6 (25.6) and 9.1 (10.0) folds higher than that of Rh/C, Pt NCs/C, Pd NCs/C and Ru NCs/C, demonstrating that the surface chalcogenation of metal NCs can indeed enhance the NRR catalysis.

Conclusion

In conclusion, we have shown that the surface chalcogenation of metal NCs as a highly promising general strategy for synthesizing highly active, FE and stable electrocatalysts for electrochemical NH_3

production at ambient conditions. Compared with pure metal NCs, the synergy effect of evident enhancement of N_2 adsorption and the substantial suppression of HER process leads to the pronounced increase of the catalytic activity of chalcogenated metal NCs. Consequently, the optimized Rh-Se NCs/C shows the outstanding performance for NRR at ambient conditions, which exhibits superior NH_3 production rate of up to 175.6 mg h^{-1} g^{-1}_{Rh} at -0.10 V vs. RHE in 0.10 M HCl, about 16.0 folds higher than that of Rh NCs/C. Moreover, the Rh-Se NCs/C substantially maintains the stable performance, morphology and composition after 18 h durability test and consecutive recycling tests. DFT calculations indicate that, the lower valence Rh-sites on the Rh-Se NCs surface exhibit substantially high efficiency for p-d coupled electron-transfer, which is the major forces to further activate and boost-up the electronic activities for $N \equiv N$ bond cleavage with highly efficient hydrogenation. Driven by the amorphous RhSe shell strain effect, a close positive correlation between catalytic and electronic activities are found in terms of volcano plot. This subtle interplay confirms the newer strategy towards improving NRR performance of metal-based electrocatalyst. This universal modulation strategy in enhancing electroactivity is of great significance for developing efficient and highly active metal-based nanocatalysts for NRR electrocatalysis and beyond in sustainable energy applications.

Methods

Synthesis of Rh NCs. In a typical synthesis of Rh NCs, 6.9 mg rhodium (iii) chloride ($RhCl_3$), 18 mg phenol (C_6H_6O), 10 mg polyvinylpyrrolidone (PVP, molecular weight 58000) and 10 mL ethylene glycol (EG) were added into a vial (volume: 30 mL). After the vial had been capped, the mixture was ultrasonicated for around 0.5 h. The resulting homogeneous mixture was heated from room temperature to 180 °C for around 0.5 h and kept at 180 °C for 5 h in an oil bath. After cooling to room temperature, the colloidal products were collected by centrifugation and washed with ethanol/acetone mixture.

Synthesis of Rh-S, Rh-Se and Rh-Te NCs. In a typical synthesis of Rh-Se NCs, the mixture of 2.1 mg H_2SeO_3 and 100 μL EG was added into the above Rh NCs solution. The mixture was then heated from room temperature to 180 °C for around 0.5 h and kept at 180 °C for 3 h in an oil bath. After cooling to room temperature, the products were collected by centrifugation and washed with ethanol/acetone mixture. The synthetic procedures for Rh-S and Rh-Te NCs were the same to that of Rh-Se NCs except for changing H_2SeO_3 with CH_4N_2S and H_6TeO_6, respectively.

Synthesis of Se NCs/C. Se powder and VC-X72 carbon were mixed in 10 mL ethanol and sonicated for 0.5 h to deposit NCs on carbon. The products were separated by centrifugation and washed with ethanol/acetone three times.

Synthesis of Pt, Pd and Ru NCs. In a typical synthesis of Pt NCs, 8.8 mg platinum (ii) chloride ($PtCl_2$), 18 mg C_6H_6O, 10 mg PVP, and 10 mL EG were added into a vial (volume: 30 mL). After the vial had been capped, the mixture was ultrasonicated for around 0.5 h. The resulting homogeneous mixture was heated from room temperature to 180 °C for around 0.5 h and kept at 180 °C for 5 h in an oil bath. The synthetic procedures for Pd and Ru NCs were the same to that of Pt NCs, except for changing $PtCl_2$ with palladium (ii) chloride ($PdCl_2$) and ruthenium (iii) chloride ($RuCl_3$), respectively.

Synthesis of Pt-Se, Pd-Se and Ru-Se NCs. In a typical synthesis of Pt-Se NCs, the mixture of 2.1 mg H_2SeO_3 and 100 μL EG was added into the above Pt NCs solution. The mixture was then heated from room temperature to 180 °C for around 0.5 h and kept at 180 °C for 3 h in an oil bath. After cooling to room temperature, the colloidal products were collected by centrifugation, and washed with ethanol/acetone mixture. The synthetic procedures for Pd-Se and Ru-Se NCs were the same to that of Pt-Se NCs, except for changing Pt NCs with Pd NCs and Ru NCs, respectively.

Preparations of supported catalysts. NCs and VC-X72 carbon were mixed in 10 mL ethanol and sonicated for 0.5 h to deposit NCs on carbon. The products were separated by centrifugation and washed with ethanol/acetone three times.

Electrochemical Measurement. N_2 reduction experiments were carried out in a two-compartment cell under ambient condition, which was separated by the Nafion 211 membrane. The Nafion 211 membrane was pretreated with 5% H_2O_2 solution and 10% H_2SO_4 for 1 h at 80 ºC, respectively, and deionized water for another 1 h. Electrochemical data were collected with a CHI 1000 electrochemical workstation. Three electrode system was used in the electrochemical measurement and the three electrodes arrangement consisted of a graphite rod as the counter electrode, saturated calomel electrode (SCE) as the reference electrode and a glassy carbon electrode. For the working electrode preparation, 2.5 mg Rh-Se NCs/C was dispersed in 0.5 mL of isopropanol and 5 μL Nafion solution. The mixture was sonicated thoroughly to form uniform catalyst ink. 20 μL of the resulting catalyst ink was drop-casted onto a glassy carbon electrode (0.196 cm^2). For N_2 reduction experiments, chronoamperometry test was conducted in N_2 saturated 0.10 M HCl solution (30 mL) (the HCl electrolyte was purged with N_2 for 30 min before the measurement.). Pure N_2 (99.99 % purity) was introduced to the cathodic compartment using properly positioned spargers so that the whole cathode was hit by the gas bubbles (flow rate: 30 ml min^{-1}). The stability test was performed by replacing the electrolyte every 2 hours without changing the electrode and Nafion membrane.

Determination of NH_3. NH_3 concentration was detected by a salicylic acid analysis method using the UV-vis spectrophotometry. In detail, 2 mL electrolyte was obtained from the cathodic chamber and with 50 μL oxidizing solution containing NaClO (ρ_{Cl} = 4-4.9), 2 mL coloring solution containing 0.4 M salicylic acid ($C_7H_6O_3$), 1.0 M NaOH, and 0.2 M trisodium citrate dihydrate ($C_6H_9Na_3O_9$) and 200 μL

catalyst solution (1 wt% $Na_2[Fe(CN)_5NO]$) for 1 h. Absorbance measurements were performed at λ = 655 nm. The concentration-absorbance curve was calibrated using the standard NH_4Cl solution with NH_4^+ concentrations of 0.0, 0.025, 0.05, 0.075, 0.1, 0.125, 0.15, 0.175, 0.2, 0.3, and 0.5 μg mL^{-1} in 0.10 M HCl. The fitting curve ($y = 0.1664x - 0.0004$, $R^2 = 0.998$) showed a good linear relation of absorbance value with the NH_3 concentration by three times independent calibrations.

Determination of N_2H_4. N_2H_4 production was estimated using the method of Watt and Chrisp. A mixed solution of 5.99 g 4-dimethylaminobenzaldehyde ($C_9H_{11}NO$), 30 mL HCl and 300 mL ethanol was used as the color reagent. In detail, 5 mL electrolyte was obtained from the cathodic chamber and added into 5 mL prepared color reagent. The absorbance of the resulting solution was measured at a wavelength of 455 nm. The concentration-absorbance curve was calibrated using the standard N_2H_4 solution with N_2H_4 concentrations of 0.0, 0.1, 0.2, 0.3, 0.4 and 0.5 μg mL^{-1} in 0.10 M HCl. The fitting curve ($y = 0.786x + 0.0279$, $R^2 = 0.999$) showed a good linear relation of absorbance value with the N_2H_4 concentration by three times independent calibrations.

Determination of NH_3 yield rate and the calculation of FE: NH_3 yield and FE_{NH3} were calculated using the following equation:

$$NH_3 \text{ yield} = (17 \times C_{NH3} \times V) / (t \times m)$$

$$FE_{NH3} = (3 \times F \times C_{NH3} \times V) / Q$$

where F is the Faraday constant (96,485 C mol^{-1}), t is the electrolysis time (2 h), m is the metal mass of the catalysts (20 μg), Q is the total charge passed through the electrode, V is the volume of the electrolyte, and C_{NH3} is the measured ammonia concentration.

Determination of the calculation of H_2 FE: The H_2 yields were analyzed by gas chromatography (GC, Agilent 7890B) with thermal conductivity detector. H_2 FE = $(2 \times F \times n_{H2}) / Q$

Computational Details: We performed DFT + U calculations with CASTEP code.[35] In this framework, the rotationally invariant (Anisimov type) DFT + U functional[37] has been used and the Hubbard U parameter is self-consistently determined for the pseudized Rh-4d and Se-4p orbital by our new linear response method.[37-44] The geometry optimization used the Broyden-Fletcher-Goldfarb-Shannon (BFGS) algorithm through all calculations. The PBE functional was chosen for PBE + U calculations with a kinetic cutoff energy of 750 eV, with the valence electron states expressed in a plane-wave basis set. The ensemble DFT (EDFT) method of Marzari et al.[45] is used for convergence on the transition metal contained compounds.

For a realistic local short-range ordered structure, a fixed volume NVT ensemble has been used for ab-initio molecular dynamics (AIMD) to conduct an analogue anneal-to-quench process from 1600 K to 300 K. All AIMD simulations have been performed onto the RhSe lattice with 128 atoms (i.e. $Rh_{64}Se_{64}$). We further built the Rh-Se NCs surface model with 64-atom Rh (100) surface lattice with four-layer thick. The vacuum thickness is set to be 15 Å. The reciprocal space integration was performed using the mesh of $2 \times 2 \times 1$[46] with Gamma-center-off, which was self-consistently selected for total energy minimization. With these special *k*-points, the total energy is converged to less than 5.0×10^{-7} eV per atom. The Hellmann-Feynman forces on the atom were converged to less than 0.001 eV/Å.

The Rh and Se norm-conserving pseudopotentials are generated using the OPIUM code in the Kleinman-Bylander projector form,[47] and the non-linear partial core correction[48] and a scalar relativistic averaging scheme[49] are used to treat the spin-orbital coupling effect. For this treatment, we similarly choose non-linear core correction technique for correcting the valence-core charge density

overlapping in such heavy fermions elements, the detail discussion of such method has been presented in previous work.[37-38] In particular, we treated the (4*d,* 5*s*, 5*p*) and (5*s*, 5*p*) states as the valence states of both Rh and Se atoms. The RRKJ method is chosen for the optimization of the pseudopotentials.[50]

For all of the electronic state calculations, we use the self-consistent determination for the U correction on the localized d orbitals to correct the on-site Coulomb energy of the electron spurious self-energy. By that method, the Hubbard U parameters on Rh-4d orbtial to be U_d = 3.03 eV, and U_p = 2.26 eV for Se-4p within Rh-Se NCs system.

References

1. J. G. Chen, *et. al.* Beyond Fossil Fuel-Driven Nitrogen Transformations. *Science* **360**, eaar6611 (2018).

2. K. C. MacLeod, P. L. Holland, Recent Developments in the Homogeneous Reduction of Dinitrogen by Molybdenum and Iron. *Nat. Chem.* **5**, 559–565 (2013).

3. K. A. Brown, *et. al.* Light-Driven Dinitrogen Reduction Catalyzed by a CdS: Nitrogenase MoFe Protein Biohybrid. *Science* **352**, 448–450 (2016).

4. Gruber, N, Galloway, J. N, An Earth-System Perspective of the Global Nitrogen Cycle. *Nature* **451,** 293–296 (2008).

5. T. Spatzal, K. A. Perez, O. Einsle, J. B. Howard, D. C. Rees, Ligand Binding to the FeMo-Cofactor: Structures of CO-Bound and Reactivated Nitrogenase. *Science* **345**, 1620–1623 (2014).

6. X. Li, *et. al.* Boosted Electrocatalytic N_2 Reduction to NH_3 by Defect-Rich MoS_2 Nanoflower. *Adv. Energy Mater.* **8**, 1801357 (2018).

7. M. Kitano, *et. al.* Ammonia Synthesis Using a Stable Electride as an Electron Donor and Reversible Hydrogen Store. *Nat. Chem.* **4**, 934–940 (2012).

8. C. J. M. Van Der Ham, M. T. M. Koper, D. G. H. Hetterscheid, Challenges in Reduction of Dinitrogen by Proton and Electron Transfer. *Chem. Soc. Rev.* **43**, 5183–8191 (2014).

9. L. Li, *et. al.* Two-Dimensional Mosaic Bismuth Nanosheets for Highly Selective Ambient Electrocatalytic Nitrogen Reduction. *ACS Catal.* **9**, 2902–2908 (2019).

10. Y. Fang, *et. al.* High-Performance Electrocatalytic Conversion of N_2 to NH_3 Using Oxygen-Vacancy-Rich TiO_2 in Situ Grown on Ti_3C_2Tx MXene. *Adv. Energy Mater.* 1803406 (2019).

11. N. Cao, G. Zheng, Aqueous Electrocatalytic N_2 Reduction under Ambient Conditions. *Nano Res.* **11,** 2992–3008. (2018).

12. Y. Liu, *et. al.* Dramatically Enhanced Ambient Ammonia Electrosynthesis Performance by In-Operando Created Li-S Interactions on MoS_2 Electrocatalyst. *Adv. Energy Mater.* 1803935 (2019).

13. Y. Luo, *et. al.* Efficient Electrocatalytic N_2 Fixation with MXene under Ambient Conditions. *Joule* **3,** 279–289. (2019).

14. S. L. Foster, *et. al.* Catalysts for Nitrogen Reduction to Ammonia. *Nat. Catal.* **1**, 490–500 (2018).

15. M. Wang, *et. al.* Over 56.55% Faradaic Efficiency of Ambient Ammonia Synthesis Enabled by Positively Shifting the Reaction Potential. *Nat. Commun.* **10**, 341 (2019).

16. C. Guo, J. Ran, A. Vasileff, S. Qiao, Rational Design of Electrocatalysts and Photo (Electro) Catalysts for Nitrogen Reduction to Ammonia (NH_3) under Ambient Conditions. *Energy Environ. Sci.* **11,** 45–56 (2018).

17. J. Deng, J. A. Iniguez, C. Liu, Electrocatalytic Nitrogen Reduction at Low Temperature. *Joule* **2**, 846–856 (2018).

18. S. Li, *et. al.* Amorphizing of Au Nanoparticles by CeO_x-RGO Hybrid Support towards Highly Efficient Electrocatalyst for N_2 Reduction under Ambient Conditions. *Adv. Mater.* **29**, 1700001 (2017).

19. H. Tao, *et. al.* Nitrogen Fixation by Ru Single-Atom Electrocatalytic Reduction. *Chem* **5**, 204–214 (2019).

20. Z. Geng, *et. al.* Achieving a Record-High Yield Rate of 120.9 for N_2 Electrochemical Reduction over Ru Single-Atom Catalysts. *Adv. Mater.* **30**, 1803498 (2018).

21. M. Shi, *et. al.* Anchoring PdCu Amorphous Nanocluster on Graphene for Electrochemical Reduction of N_2 to NH_3 under Ambient Conditions in Aqueous Solution. *Adv. Energy Mater.* **8**, 1800124 (2018).

22. H. Liu, *et. al.* Surfactant-Free Atomically Ultrathin Rhodium Nanosheet Nanoassemblies for Efficient Nitrogen Electroreduction. *J. Mater. Chem. A* **6,** 3211–3217 (2018).

23. S. Chen, *et. al.* Electrocatalytic Synthesis of Ammonia at Room Temperature and Atmospheric Pressure from Water and Nitrogen on a Carbon-Nanotube-Based Electrocatalyst. *Angew. Chem. Int. Ed.* **56**, 2699–2703 (2017).

24. N. Zhang, *et. al.* Refining Defect States in $W_{18}O_{49}$ by Mo Doping: A Strategy for Tuning N_2 Activation towards Solar-Driven Nitrogen Fixation. *J. Am. Chem. Soc.* **140**, 9434–9443 (2018).

25. Z. Wang, *et. al.* Electrocatalytic Hydrogenation of N_2 to NH_3 by MnO: Experimental and Theoretical Investigations. *Adv. Sci.* **6**, 1801182 (2019).

26. W. Qiu, *et. al.* High-Performance Artificial Nitrogen Fixation at Ambient Conditions using a Metal-Free Electrocatalyst. *Nat. Commun.* **9**, 3485 (2018).

27. Y. Liu, *et. al.* Facile Ammonia Synthesis from Electrocatalytic N_2 Reduction under Ambient Conditions on N-Doped Porous Carbon. *ACS Catal.* **8,** 1186−1191 (2018).

28. L. Zhang, L. Ding, G. Chen, X. Yang, H. Wang, Ammonia Synthesis under Ambient Conditions: Selective Electroreduction of Dinitrogen to Ammonia on Black Phosphorus Nanosheets. *Angew. Chem. Int. Ed.* **131**, 2638−2642 (2019).

29. X. Min, M. W. Kanan, Pd-Catalyzed Electrohydrogenation of Carbon Dioxide to Formate: High Mass Activity at Low Overpotential and Identification of the Deactivation Pathway. *J. Am. Chem. Soc.* **137**, 4701−4708 (2015).

30. R. Chen, *et. al.* Nanoparticle Surface Characterization and Clustering through Concentration-Dependent Surface Adsorption Modeling. *ACS Nano* **8,** 9446−9456 (2014).

31. D. Kong, H. Wang, Z. Lu, Y. Cui, $CoSe_2$ Nanoparticles Grown on Carbon Fiber Paper: An Efficient and Stable Electrocatalyst for Hydrogen Evolution Reaction. *J. Am. Chem. Soc.* **136**, 4897−4900 (2014).

32. J. Wu, *et. al.* Revealing the Synergistic Effects of Rh and Substituted $La_2B_2O_7$ (B = Zr or Ti) for Preserving the Reactivity of Catalyst in Dry Reforming of Methane. *ACS Catal.* **9**, 932−945 (2019).

33. H. Huang, *et. al.* Understanding of Strain Effects in the Electrochemical Reduction of CO_2: Using Pd Nanostructures as an Ideal Platform. *Angew. Chem. Int. Ed.* **129**, 3648−3652 (2017).

34. D. Kim, J. Resasco, Y. Yu, A. M. Asiri, P. Yang, Synergistic Geometric and Electronic Effects for Electrochemical Reduction of Carbon Dioxide using Gold-Copper Bimetallic Nanoparticles. *Nat. Commun.* **5**, 4948 (2014).

35. S. J. Clark, *et. al.* First Principles Methods using CASTEP. *Zeitschrift Fur Kristallographie* **220,** 567−570 (2015).

36. I. A. Vladimir, F. Aryasetiawan, A. I. Lichtenstein. First-Principles Calculations of the Electronic Structure and Spectra of Strongly Correlated Systems: The LDA + U Method. *J. Phys. Condens. Matter* **9**, 767–808 (1997).

37. B. Huang, R. Gillen, J. Robertson, Study of CeO_2 and Its Native Defects by Density Functional Theory with Repulsive Potential. *J. Phys. Chem. C* **118**, 24248–24256 (2014).

38. B. Huang, Superiority of DFT + U with Non-Linear Core Correction for Open-Shell Binary Rare-Earth Metal Oxides: A Case Study of Native Point Defects in Cerium Oxides. *Philosophical Magazine* **94**, 3052–3071 (2014).

39. B. Huang, 4f Fine-Structure Levels as the Dominant Error in the Electronic Structures of Binary Lanthanide Oxides. *J. Comput. Chem.* **37**, 825–835 (2016).

40. B. Huang, Intrinsic Deep Hole Trap Levels in Cu_2O with Self-Consistent Repulsive Coulomb Energy. *Solid State Commun.* **230**, 49–53 (2016).

41. B. Huang, Strong Compensation Hinders the p-Type Doping of ZnO: A Glance over Surface Defect Levels. *Solid State Commun.* **237–238**, 34–37 (2016).

42. B. Huang, Unraveling Energy Conversion Modeling in the Intrinsic Persistent Upconverted Luminescence of Solids: A Study of Native Point Defects in Antiferromagnetic Er_2O_3. *Phys. Chem. Chem. Phys.* **18**, 13564–13582 (2016).

43. B. Huang, The Screened Pseudo-Charge Repulsive Potential in Perturbed Orbitals for Band Calculations by DFT + U. *Phys. Chem. Chem. Phys.* **19**, 8008–8025 (2017).

44. J. Hu, *et. al.* Engineering Stepped Edge Surface Structures of MoS_2 Sheet Stacks to Accelerate the Hydrogen Evolution Reaction. *Energy & Environmental Science* **10**, 593–603 (2017).

45. N. Marzari, D. Vanderbilt, M. C. Payne, Ensemble Density-Functional Theory for *Ab Initio* Molecular Dynamics of Metals and Finite-Temperature Insulators. *Phys. Rev. Lett.* **79**, 1337–1340 (1997).

46. M. I. J. Probert, M. C. Payne, Improving the Convergence of Defect Calculations in Supercells: An *ab initio* Study of the Neutral Silicon Vacancy. *Phys. Rev. B* **67**, 075204 (2003).

47. L. Kleinman, D. M. Bylander, Efficacious Form for Model Pseudopotentials. *Phys. Rev. Lett.* **48**, 1425–1428 (1982).

48. S. G. Louie, S. Froyen, M. L. Cohen, Nonlinear Ionic Pseudopotentials in Spin-Density-Functional Calculations. *Phys. Rev. B* **26**, 1738–1742 (1982).

49. I. Grinberg, N. J. Ramer, A. M. Rappe, Transferable Relativistic Dirac-Slater Pseudopotentials. *Phys. Rev. B* **62**, 2311–2314 (2000).

50. A. M. Rappe, K. M. Rabe, E. Kaxiras, J. D. Joannopoulos, Optimized Pseudopotentials. *Phys. Rev. B* **41**, 1227–1230 (1990).

Acknowledgement

This work was financially supported by the Ministry of Science and Technology (2016YFA0204100, 2017YFA0208200), the National Natural Science Foundation of China (21571135), Young Thousand Talented Program, Jiangsu Province Natural Science Fund for Distinguished Young Scholars (BK20170003), the Priority Academic Program Development of Jiangsu Higher Education Institutions (PAPD), and the start-up supports from Soochow University.

Author contributions

X.H. conceived and supervised the research. X.H., C.Y. and S.B. designed the experiments. X.H., C.Y., S.B., Y.F., T.Z. and Q.S. performed most of the experiments and data analysis. B.H. performed the

theoretical computations and analyzed the theoretical results. X.H., C.Y., S.B., Y.F. T.Z. and Q.S. participated in various aspects of the experiments and discussions. X.H., C.Y. and S.B. wrote the paper. All authors discussed the results and commented on the manuscript.

Additional information

Supplementary Information is linked to the online version of this paper at http://www.nature.com/.

Competing financial interests

The authors declare no competing financial interests.

Reprint and permissions information is available at http://www.nature.com/.

Correspondence and requests for materials should be addressed to B.H. (bhuang@polyu.edu.hk) or X.H. (hxq006@suda.edu.cn).

Figures

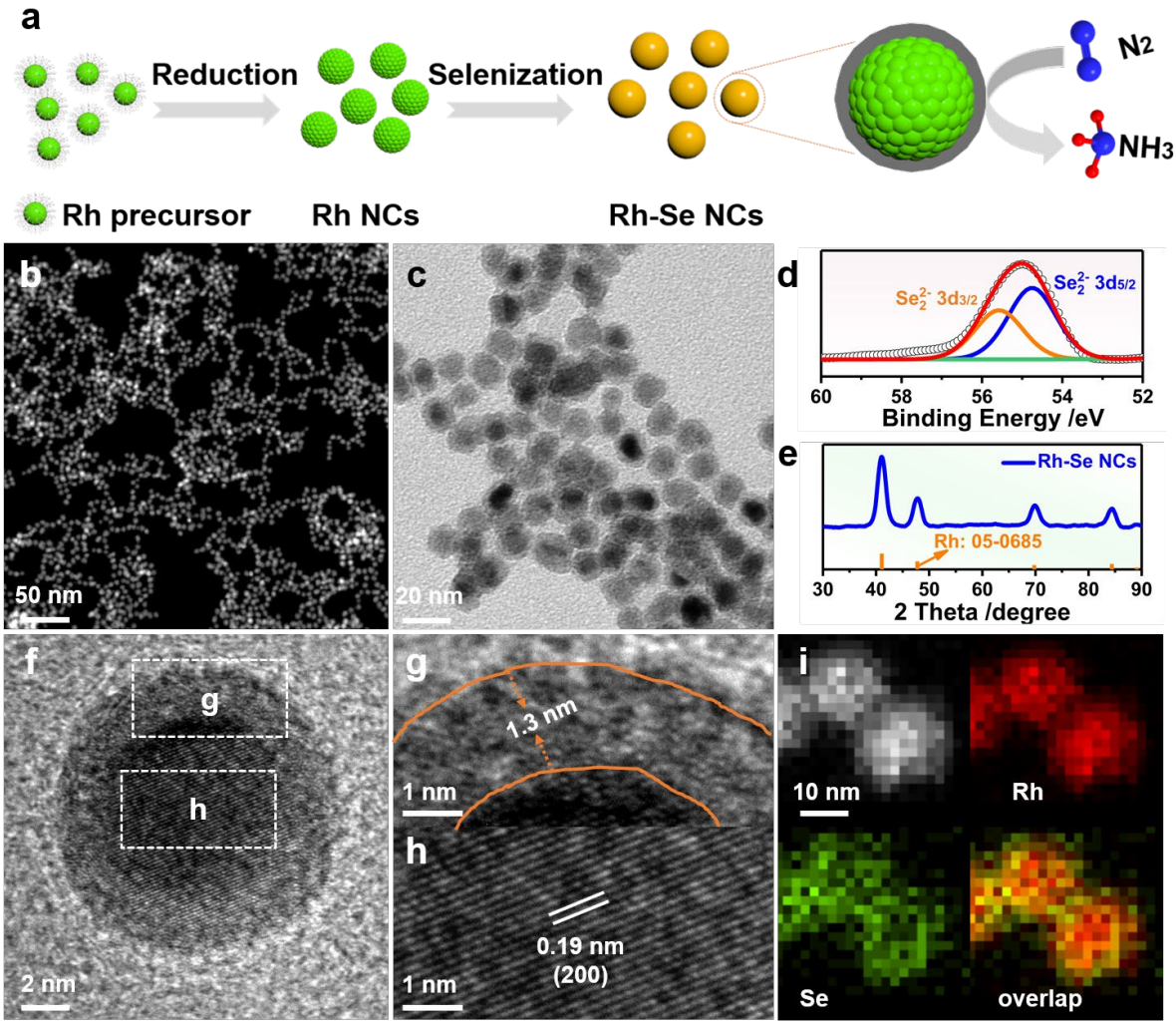

Figure 1. Morphology and structural characterization of Rh-Se NCs. (**a**) Schematic illustration of the synthetic process of Rh-Se NCs/C. (**b**) HAADF-STEM image, (**c**) TEM image, (**d**) Se 3d XPS pattern, (**e**) PXRD pattern, (**f**) HRTEM image, (**g**, **h**) the magnified regions in (**f**), and (**i**) HAADF-STEM image and elemental mappings of Rh-Se NCs.

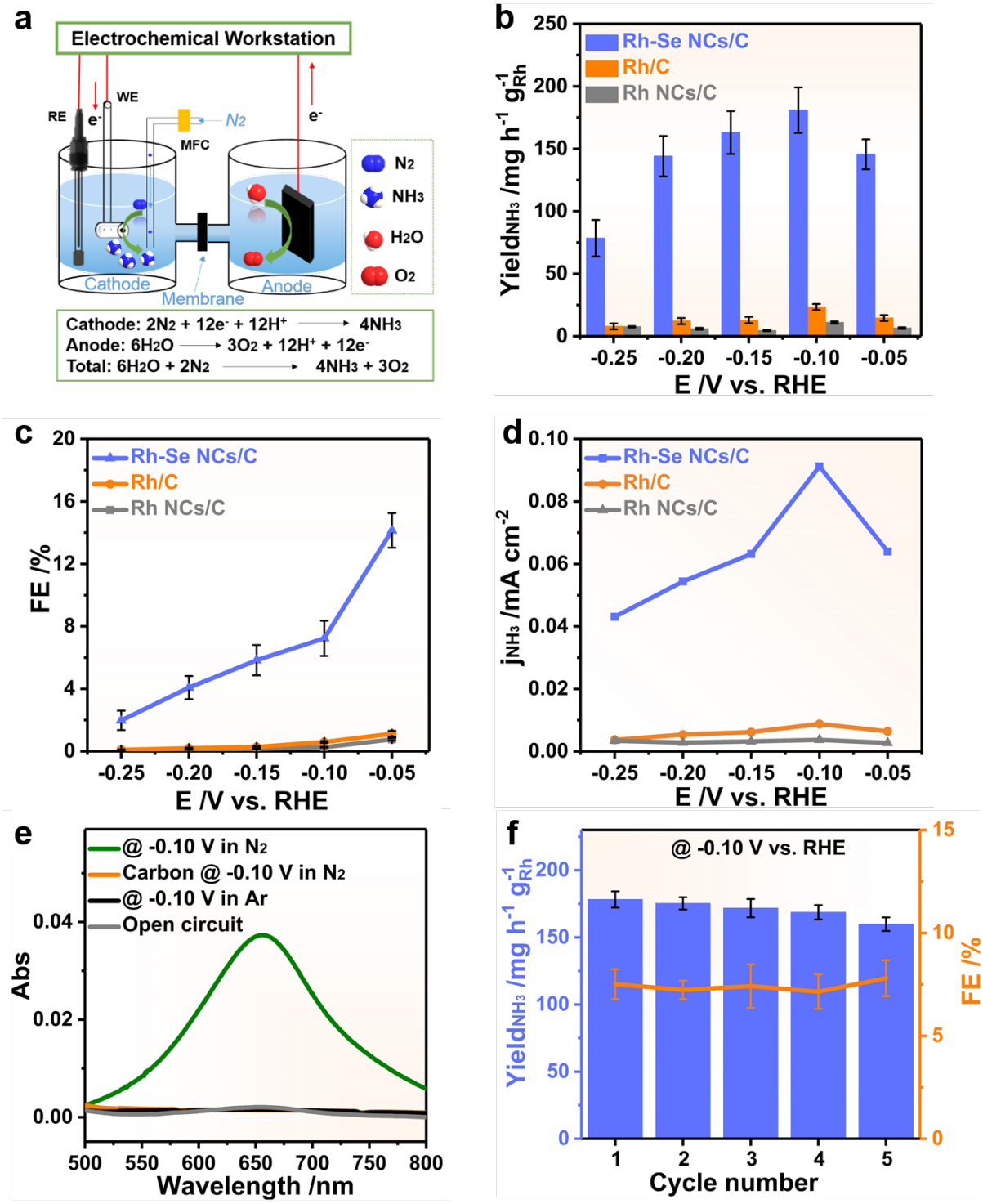

Figure 2. NRR performance of different catalysts. (**a**) Schematic for electrocatalytic NRR (MFC is mass flow controller, the membrane is Nafion 211). (**b**) The NH_3 yields, (**c**) FE and (**d**) partial current densities of Rh-Se NCs/C, Rh/C and Rh NCs/C at various applied potentials. (**e**) UV-visible absorption

spectra of the electrolyte for Rh-Se NCs/C at different conditions. (Green line for electrolyte after electrolysis at -0.10 V for 2 h in N_2-saturated 0.10 M HCl; orange line for carbon after electrolysis at -0.10 V for 2 h in N_2-saturated 0.10 M HCl; black line for electrolyte after electrolysis at -0.10 V for 2 h in Ar-saturated 0.10 M HCl; grey line for electrolyte after electrolysis at open circuit for 2 h in N_2-saturated 0.10 M HCl.) (**f**) Cycling test of Rh-Se NCs/C at -0.10 V vs. RHE.

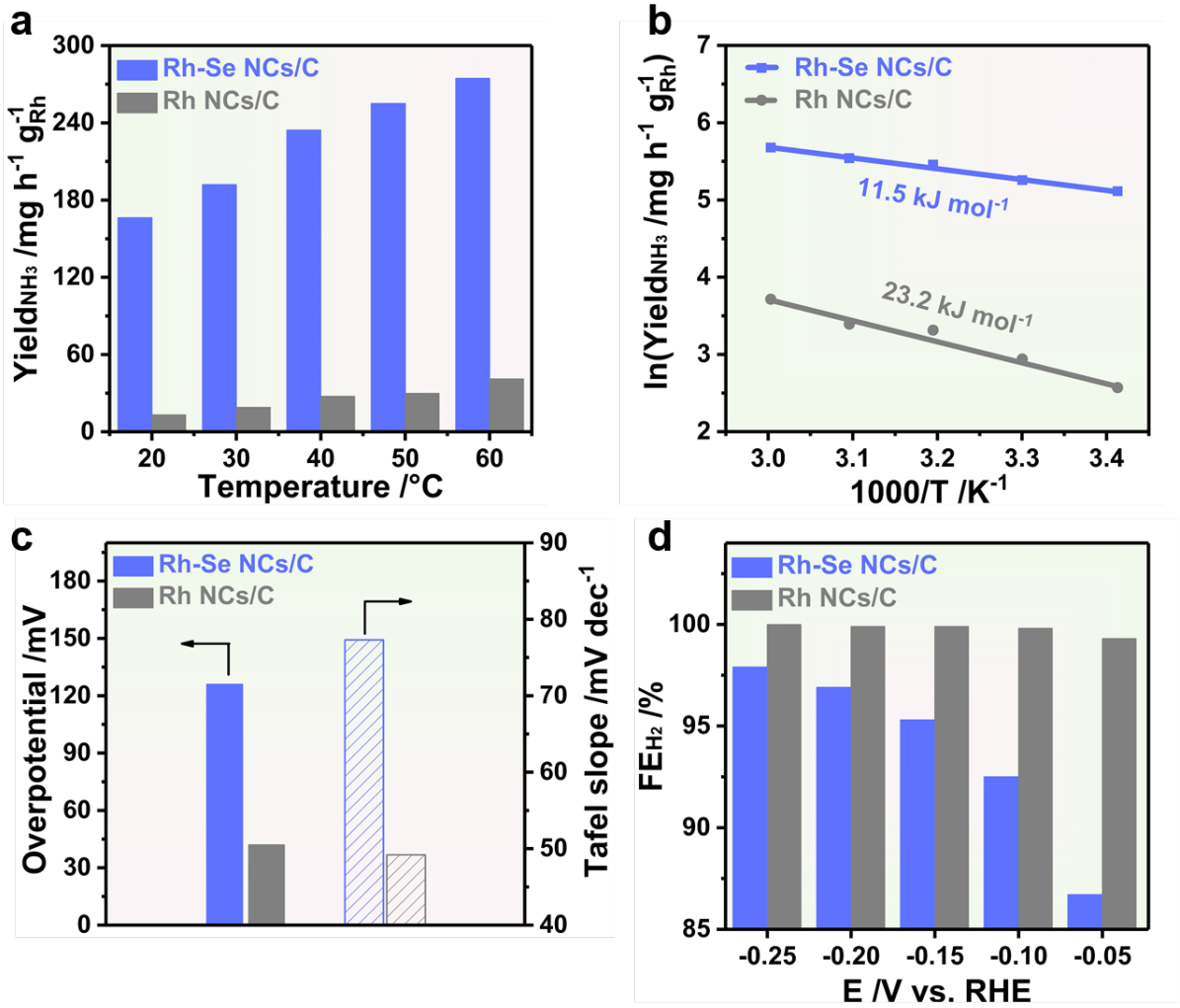

Figure 3. Surface selenation effect. (**a**) NH_3 yield from different reaction temperatures, (**b**) apparent activation energy (E_a), (**c**) overpotential and Tafel slope and (**d**) FE of H_2 from Rh NCs and Rh-Se NCs/C.

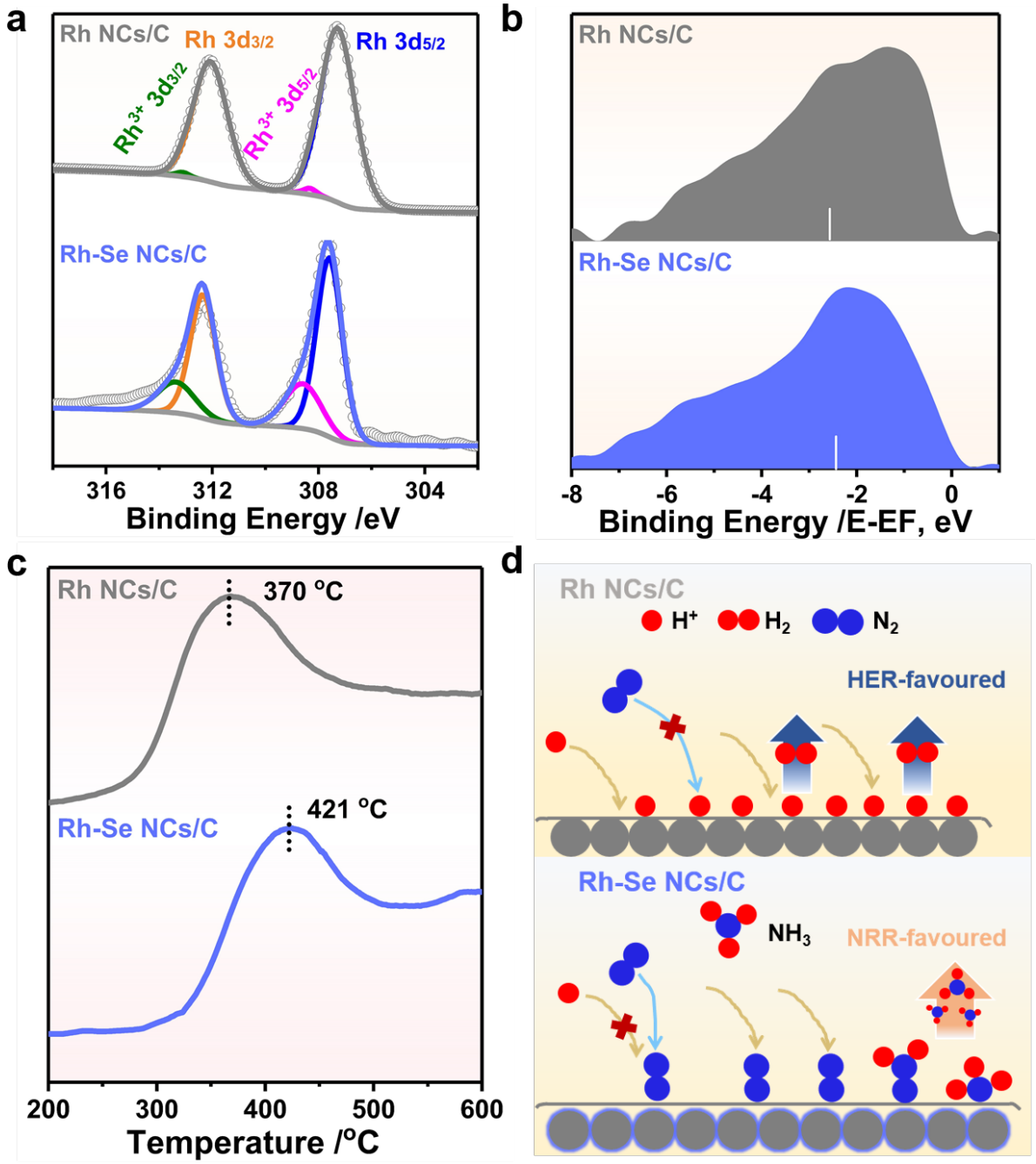

Figure 4. Surface characterization of the Rh-Se NCs/C for NH_3 synthesis. (**a**) XPS patterns of Rh 3d, (**b**) surface valence band photoemission spectra and (**c**) the N_2-TPD profiles of Rh NCs/C and Rh-Se NCs/C. (**d**) Schematic showing the proposed mechanism for NRR on the catalytic surface of the Rh NCs/C and Rh-Se NCs/C.

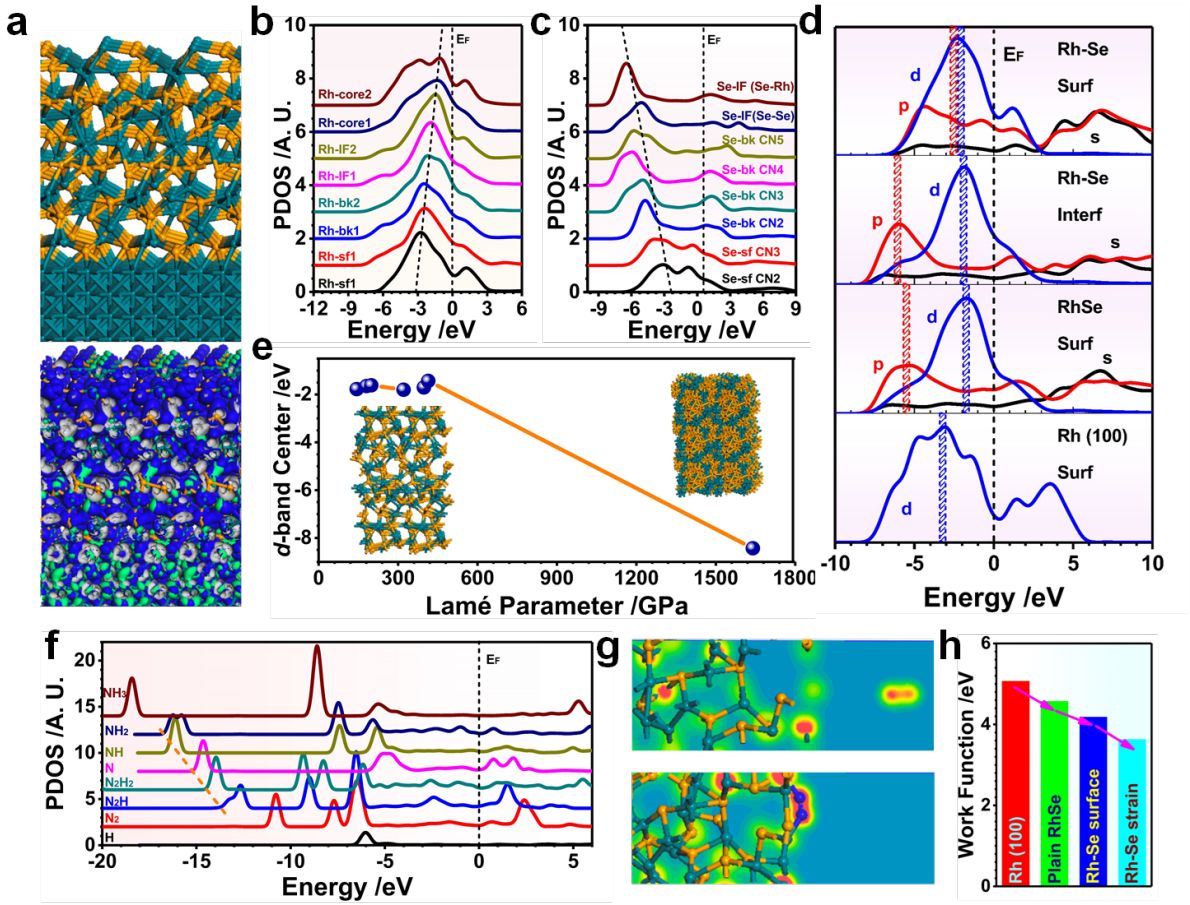

Figure 5. Electronic activities of Rh-Se NCs for NRR catalytic activity. (**a**) Overall geometry optimized Rh-Se NCs interface structure (up-panel); the real-spatial contour plots for bonding and anti-bonding orbitals near E_F (lower panel). (**b**) site-dependent PDOSs of Rh-4d band variation from in-depth Rh-core towards top surface area, via interfacial region. (**c**) site-dependent PDOSs of Se-4p band variation from in-depth interfacial selenation region towards top surface area. (**d**) PDOSs comparison among Rh (100) surface, plain amorphous RhSe surface, Rh-Se NCs interface, and Rh-Se NCs surface. (**e**) Volcano-plot for the surface strain-effect driven trends for surface catalytic and electronic activities. (**f**) Individual PDOSs analysis for intermediate adsorbing N-species. (**g**) Two-dimensional contour plots for charge densities before and after N_2-adsorption. (**h**) Work functions among Rh (100) surface, plain amorphous RhSe surface, Rh-Se NCs interface, and Rh-Se NCs surface.

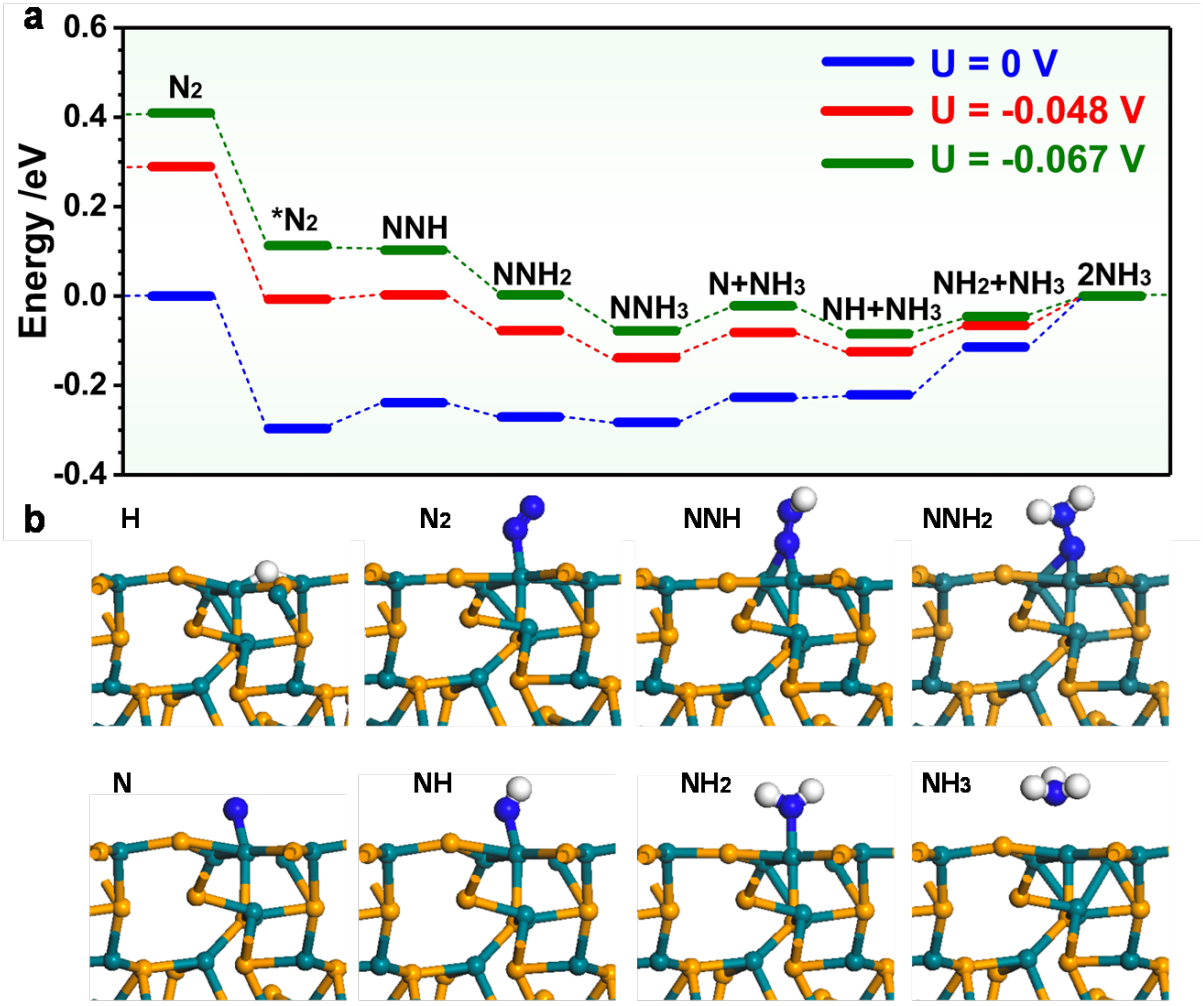

Figure 6. Energetic pathways for NRR. (**a**) Reaction pathway of acidic NRR catalysis at the potential of U = 0 V, U = -0.048 V and U = -0.067 V. (**b**) The local structural configurations for demonstrating the NRR (acidic) process within the Rh-Se NCs surface system.

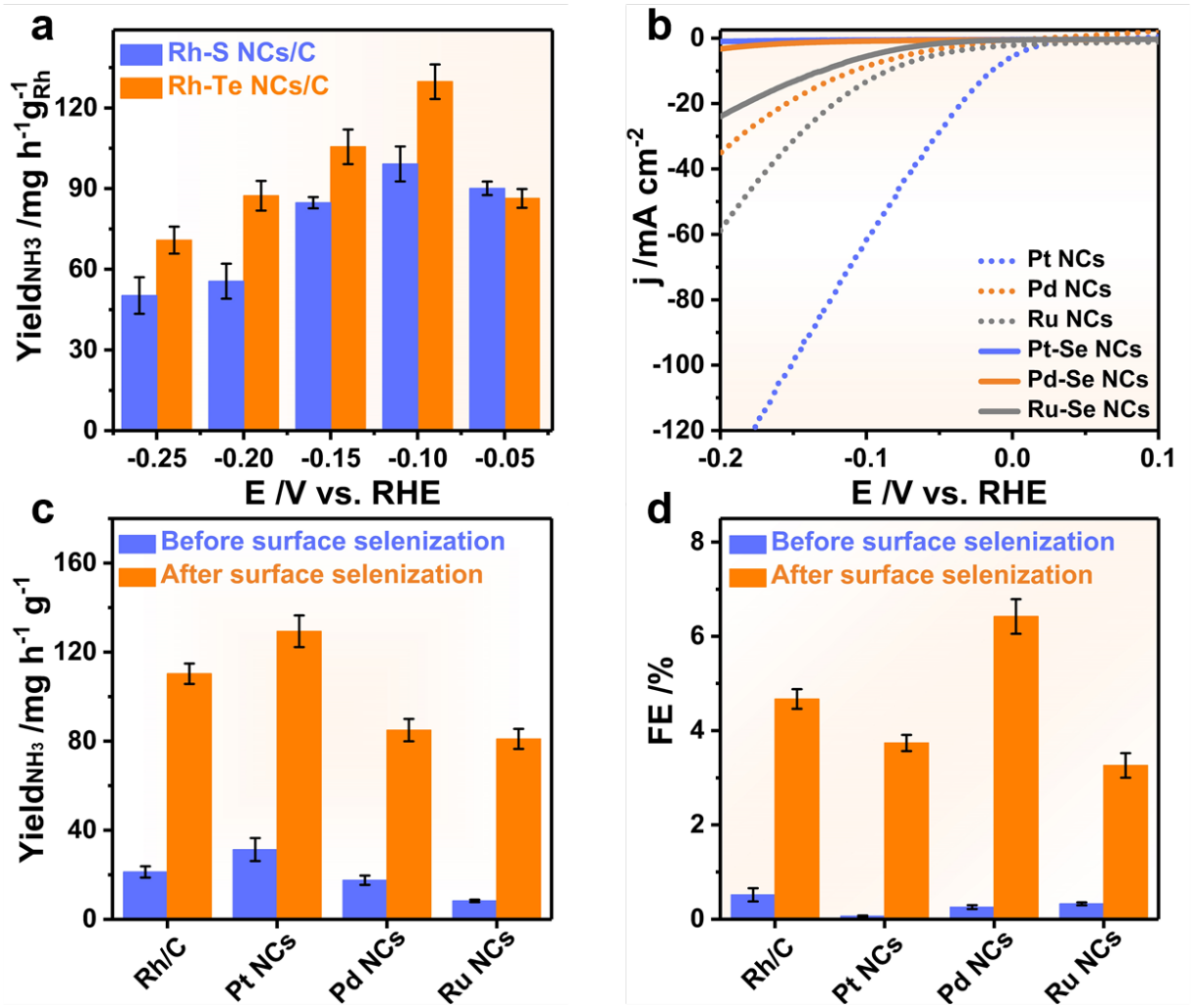

Figure 7. General strategy to boost NRR by surface chalcogenation. (**a**) The NH_3 yields and FE of Rh-S NCs/C and Rh-Te NCs/C at various applied potentials. (**b**) LSV curves in N_2-saturated 0.10 M HCl with a scan rate of 5 mV s^{-1}, (**c**) the NH_3 yield and (**d**) FE at -0.10 V vs. RHE of various catalysts.